View metadata, citation and similar papers at core.ac.uk

brought to you by CORE

provided by Purdue E-Pubs

Purdue University
Purdue e-Pubs

Birck and NCN Publications | Birck Nanotechnology Center

7-1-2011

A CAD Model for Creep Behavior of RF-MEMS Varactors and Circuits

Hao-Han Hsu
Birck Nanotechnology Center, Purdue University, hsuh@purdue.edu

Dimitrios Peroulis
Birck Nanotechnology Center, Purdue University, dperouli@purdue.edu

Follow this and additional works at: http://docs.lib.purdue.edu/nanopub

Part of the Nanoscience and Nanotechnology Commons

Hsu, Hao-Han and Peroulis, Dimitrios, "A CAD Model for Creep Behavior of RF-MEMS Varactors and Circuits" (2011). *Birck and NCN Publications.* Paper 982.
http://docs.lib.purdue.edu/nanopub/982

This document has been made available through Purdue e-Pubs, a service of the Purdue University Libraries. Please contact epubs@purdue.edu for additional information.

A CAD Model for Creep Behavior of RF-MEMS Varactors and Circuits

Hao-Han Hsu, *Student Member, IEEE*, and Dimitrios Peroulis, *Member, IEEE*

***Abstract*—In this paper, we propose a compact computer-aided design (CAD) model that may be utilized to simulate the creep behavior of RF microelectromechanical systems (RF-MEMS) varactors in RF circuits and subsystems. This model is capable of calculating the long-term response of RF-MEMS devices to an arbitrary input waveform. It is implemented using Agilent's Advanced Design System (ADS). The presented CAD model employs the generalized Voigt–Kelvin model to capture the long-term behavior of RF-MEMS devices. It is experimentally validated with measurements of Ni varactors that extend up to 760 h of constant loading. Its effectiveness is demonstrated with a tunable RF-MEMS resonator and an RF-MEMS phase shifter. The tunable resonator that consists of one $\lambda/2$ coplanar waveguide resonator and two nanocrystalline-Ni RF-MEMS varactors is fabricated and measured. S-parameters of this tunable resonator have been recorded for 80 h under a bi-state bias condition of 0 and 40 V. It is shown that the resonant frequency is shifted by 90 MHz and the varactor deformed by 0.12 μm over the 80-h period. Good agreement between the CAD model and the measurements is obtained. The impact of the duty factor of the bias signal is also discussed. The model's capability of handling arbitrary input is demonstrated on an RF-MEMS phase shifter operated with a sawtooth waveform.**

***Index Terms*—Computer-aided design (CAD) model, creep, nickel, RF microelectromechanical systems (RF MEMS), viscoelasticity.**

I. Introduction

As RF microelectromechanical systems (RF-MEMS) devices approach their market potential, understanding and modeling their failure modes becomes increasingly important. Potential reliability issues include dielectric charging [1], stiction [2], fatigue [3], contact degradation [4], and creep/viscoelasticity [5]–[10]. Computer-aided design (CAD) models that can predict the behavior of RF-MEMS devices and their circuit applications in the presence of these failure modes are on high demand.

Manuscript received January 03, 2011; accepted February 18, 2011. Date of publication May 05, 2011; date of current version July 13, 2011. This work was supported by the National Nuclear Security Administration (NNSA) Center of Prediction of Reliability, Integrity, and Survivability of Microsystems, the Department of Energy under Award DE-FC52-08NA28617, and the Defense Advanced Research Projects Agency (DARPA) Nanoelectromechanical/Microelectromechanical System Science and Technology (N/MEMS S&T) Fundamentals Program under Grant N66001-10-1-4006 issued by the Space and Naval Warfare Systems Center Pacific (SPAWAR).

The authors are with the Department of Electrical and Computer Engineering, Birck Nanotechnology Center, Purdue University, West Lafayette, IN 47907 USA (e-mail: hsuh@purdue.edu; dperouli@purdue.edu).

Color versions of one or more of the figures in this paper are available online at http://ieeexplore.ieee.org.

Digital Object Identifier 10.1109/TMTT.2011.2138154

The term creep signifies, in general, the tendency of materials such as metals and polymers to slowly deform when subject to a constant load [11]. It is also referred to as viscoelasticity because of the material's tendency to exhibit both viscous and elastic characteristics under an applied force. For example, a constant axial load applied to a beam may cause a progressively increasing axial elongation. Several researchers study these phenomena and mechanisms in detail [5]–[8]. Creep can be found in many materials widely used in RF-MEMS, including Au, Al, and Ni. Vicker-Kirby *et al.* reported anelastic phenomena in MEMS cantilever accelerometers made of Si, Ni, and Au [5] for 30 h. It was demonstrated that Ni is more resistant to creep than Au. Tuck *et al.* conducted a creep test on polysilicon beams for 600 s at 1072 K and above [6]. Electrical and mechanical failure due to dopant migration and oxidation were reported. van Gils *et al.* performed an experiment on an Al RF-MEMS switch for 15 h [7]. Yan *et al.* performed a stress-relaxation test on an Au thin film using a bulge test technique for 80 h [9]. The linearity of viscoelasticity in such films was demonstrated using a cyclic-loading test. Chasiotis *et al.* conducted an investigation into the strain-rate effects on the mechanical behavior of nanocrystalline Au films [8]. It is reported that dislocation creep might be the cause of the decrease of the maximum strength, effective Young's modulus, and yield strength in Au thin film at low strain rate. The authors experimentally studied the viscoelastic behavior in analog RF-MEMS varactors up to 1400 h [10]. Based on the long-term measurement of capacitance, the dynamic spring constant was defined to describe the long-term behavior in RF-MEMS devices.

The studies above provide insights into potential failure modes in RF-MEMS devices. However, to the authors' best knowledge, CAD models for creep/viscoelasticity that can be employed in RF-circuit design are not available in the open literature. In this paper, the authors expand their previous work on tunable RF-MEMS resonators [12] and present a CAD model for creep behavior in RF-MEMS varactors and circuits. This model calculates the time-dependent capacitance and gap of an RF-MEMS varactor under arbitrary bias voltage based on an experimentally obtained creep compliance. The model validation is done with measurements of constant loading that last up to 760 h. Two RF-MEMS circuits, a tunable resonator, and a phase shifter are employed to demonstrate the usefulness of this CAD model. The time-dependent gap and resonant frequency of the tunable RF-MEMS resonator are measured for 80 h and show good consistency to the simulation results obtained from this model. The behavior under variable duty factors of the bias signal is also studied. A phase shifter composed of transmission lines and ten RF-MEMS varactors is simulated using this model. Its creep behavior under a sawtooth

0018-9480/$26.00 © 2011 IEEE

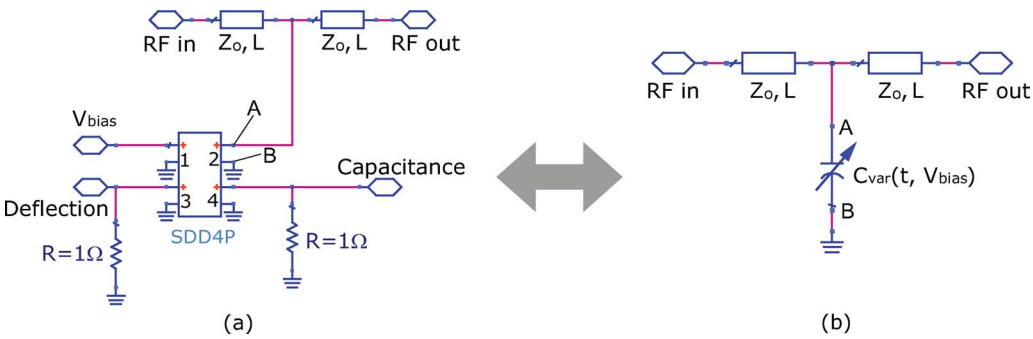

Fig. 1. Circuit schematic of the proposed CAD model. (a) Four-port ADS model. (b) Equivalent-circuit model.

input waveform is investigated. This model may be used in higher level simulations to understand the behavior of the whole system in long-term operation.

II. CAD Model for Creep

The goal of this CAD model is to show the performance change of RF circuits/sub-systems at various time points under the effects of creep. Our goal is not to distinguish between the different physical mechanisms responsible for creep. The authors rather focus on an easy-to-use model for RF design at the system and subsystem levels. Hence, a behavioral model, the generalized Voigt-Kelvin model, is adopted to simplify and speed up the simulation. This model is based on an experimentally extracted parameter called creep compliance. All mechanisms and physics behind creep, such as grain-boundary diffusion and dislocation movements, are enveloped in this creep compliance, and they are not discussed in detail in this paper.

A. Varactor Model

The creep compliance is one of the critical parameters to characterize creep. It is defined as [13]

$$D(t) = \frac{\epsilon(t)}{\sigma_o} \tag{1}$$

where $\epsilon(t)$ is the strain as a function of time and σ_o is the applied constant stress. The generalized Voigt–Kelvin model is widely used to describe a viscoelastic system of multiple time constants, which consists of elastic springs and dampers. The creep compliance of this model is given by

$$D(t) = \left[\frac{1}{E_o} + \sum_{i=1}^{n} \frac{1}{E_i}(1 - e^{-t/\tau_i})\right] \tag{2}$$

where τ_i is the ith time constant and E_i is the ith elastic modulus. The first term in (2) is the instant elasticity, and the second term represents the delayed elasticity. The response to an arbitrary stress input can be calculated using the Boltzmann superposition principle

$$\epsilon(t) = \epsilon_o + \int_0^t D(t-\xi)\frac{d\sigma(\xi)}{d\xi}d\xi \tag{3}$$

where $\epsilon(t)$ is the strain and ϵ_o is the strain at $t = 0$. The creep compliance can be considered as the unit-step response of this viscoelastic system. The convolution integral superposes the unit-step response according to the derivative of the stress input. This process accounts for the entire input history and can be used to calculate the behavior of RF-MEMS devices. By applying beam theory, it can be shown that the maximum deflection of a beam is given by

$$\delta(t) = \frac{E}{K_o}\left[F(0)D(t) + \int_{0^+}^{t} D(t-\xi)\frac{dF(\xi)}{d\xi}d\xi\right] \tag{4}$$

where E is the Young's modulus, K_o is the spring constant at $t = 0$, and $F(t)$ is the applied force.

The CAD model that consists of a four-port equation-based nonlinear component is implemented in Agilent's Advanced Design System (ADS), as shown in Fig. 1(a) [14]. Though this component is not capable of computing the convolution integral in (4) in the time domain, the frequency response of each port can be assigned to this component and thus this integral can be computed in the frequency domain. The frequency-domain expression of (4) is required in the computation of the varactor deflection. In the frequency domain, it can be rewritten as

$$\overline{\delta}(\omega) = \frac{E}{K_o}\left[j\omega\overline{D}(\omega)\cdot\overline{F}(\omega)\right] \tag{5}$$

$$\overline{D}(\omega) = \frac{1}{j\omega}\left[\frac{1}{E_o} + \sum_{i=1}^{n}\frac{1}{E_i}\left(1 - \frac{j\omega}{j\omega + 1/\tau_i}\right)\right] \tag{6}$$

where $\overline{\delta}(\omega)$, $\overline{D}(\omega)$, and $\overline{F}(\omega)$ are the corresponding Fourier transforms.

The equations of this four-port component are

$$\begin{aligned} I_1 &= 0 \\ I_2 &= \left[j\omega C_{\text{var}}(g_o - V_3)\right]V_2 \\ I_3 &= -\frac{E}{K_o}\left[j\omega\overline{D}(\omega)\cdot\overline{F}_{\text{var}}(V_1, g_o - V_3)\right] \\ I_4 &= -C_{\text{var}}(g_o - V_3) \end{aligned} \tag{7}$$

where V_n and I_n are the voltage and current of port n, g_o is the initial gap of the varactor, $C_{\text{var}}(g)$ is the capacitance of the varactor as a function of gap, and $F_{\text{var}}(V_{\text{bias}}, g)$ is the electrostatic force exerted on the varactor when the bias voltage is V_{bias} and the gap is g. The bias voltage applied to the RF-MEMS varactor is taken from port 1. The current that flows into port 1 can be any arbitrary value without altering the simulation result; therefore, it is set to zero for simplicity. Port 2 represents the electrical interface of the varactor to the RF circuit. The equivalent circuit

of this four-port model can be found in Fig. 1(b). Nodes A and B correspond to the two RF nodes of the varactor. In this case, the varactor is shunt to a transmission line. The texts "RF in" and "RF out" stand for RF input and output, respectively. The currents of ports 3 and 4 are defined as the deflection and capacitance of the varactor, respectively. The deflection at port 3 is calculated based on (4). A finite-element analysis (FEA) tool is utilized to calculate $F_{\rm var}(V_{\rm bias}, g)$ and $C_{\rm var}(g)$ to include the effects of both parasitics and fringing fields [15]. Two 1-Ω resistors are used to convert currents to voltages because these values as voltage are needed in the calculation at other ports.

For the reader's reference, the time-domain form of (7) are given by

$$\begin{aligned} I_1 &= 0 \\ I_2 &= C_{\rm var}(g_o - V_3)\frac{dV_2}{dt} \\ I_3 &= \frac{E}{K_o}F_{\rm var}\left(V_1(0), g_o\right)D(t)) \\ &\quad + \frac{E}{K_o}\int_{0+}^{t} D(t-\xi)\frac{dF_{\rm var}\left(V_1(\xi), g_o - V_3(\xi)\right)}{d\xi}d\xi \\ I_4 &= -C_{\rm var}(g_o - V_3) \end{aligned} \tag{8}$$

where $C_{\rm var}(g)$ is the varactor capacitance when the gap equals g, E is the Young's Modulus, K_o is the spring constant at $t = 0$, $D(t)$ is the creep compliance, $F_{\rm var}(V, g)$ is the electrostatic force exerted on the varactor, and g is the gap of the varactor.

B. Model Validation

The model validation is carried out by comparing the simulated deflection and capacitance with the experimental data obtained from an analog RF-MEMS varactor. While the model validation is done with Ni varactors, any material system that can be described by the Voigt–Kelvin model can be modeled in a similar way.

The fabricated Ni RF-MEMS varactor is shown in Fig. 2(a) and the cross section is illustrated in Fig. 2(b) [10]. It consists of a 300 μm $\times$ 220 μm Ni top plate and three Au bottom electrodes. The 3-μm-thick top plate is suspended using four symmetric suspension beams of about 200-μm long. The initial gap between the top and bottom electrodes is about 3 μm. The top plate is electrically grounded, and the bias voltage is applied to the two electrodes at the sides. The center electrode is designed for capacitance sensing. The measured pull-in voltage of this varactor is approximately 44 V. No dielectric layers exist between the bottom electrodes and the Ni structure. In order to prevent the varactor from being pulled in, the applied voltage is kept lower than this pull-in voltage during the measurements.

The capacitance of the varactor is measured using the AD7746 circuit from Analog Devices at room temperature under the ambient pressure of 1 atm.[1] It is a high-precision capacitance-to-digital converter (CDC) composed with a 24-bit $\Delta - \Sigma$ modulator and a third-order digital filter. Careful shielding and grounding is performed to minimize the measurement noise and maximize the accuracy. The measurement

[1]AD7746 Capacitance to Digital Converter, Analog Devices Inc., Norwood, MA. [Online]. Available: http://www.analog.com

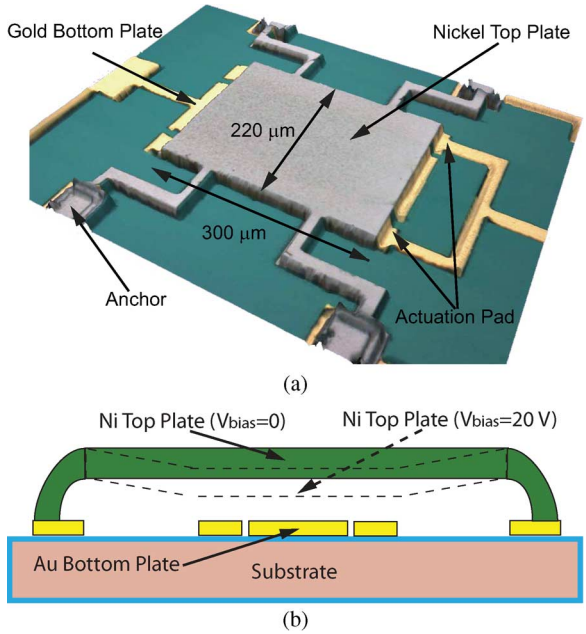

Fig. 2. (a) Confocal microscope image of the fabricated analog RF-MEMS varactor. The gap between the Ni plate and Au electrodes is 3 μm. There are no dielectric layers in this varactor. (b) Cross section of the RF-MEMS varactor. The positions of the Ni top plate at $V_{\rm bias} = 0$ and 20 V are depicted in solid and dashed line, respectively.

uncertainty is less than 200 aF [10]. A special bi-state bias condition is employed to reveal the creep behavior of the RF-MEM varactors. In the first state, the varactor is biased at a constant voltage of 20 V for 60 min and its capacitance is constantly being recorded at a rate of 5 samples/s. This voltage may be an arbitrary value as long as it is lower than the pull-in voltage. However, since the varactor gap decreases over time due to creep and may be pulled in after a certain amount of time, the authors set the bias voltage around half of the pull-in voltage to avoid the potential risk. The bias voltage is removed for 1 min in the second state and its capacitance is recorded as well. This cycle is repeated for 760 h.

The creep compliance used in (7) is extracted from the aforementioned varactor measurement and is plotted in Fig. 3. This creep compliance is significantly extended to 760 h from the one reported in [12]. These two creep compliances are in good agreement in spite of the small differences in the time constants caused by common batch-to-batch fabrication tolerances. The procedure to obtain the creep compliance can be summarized as follows. First, the gap and the electrostatic force of the varactor need to be extracted from the measurement. This is accomplished with an FEA code [15]. Second, based on (2), a hypothetical gap is calculated using the Boltzmann superposition principle shown in (4). Third, the parameters E_i and τ_i in (2) are adjusted until this hypothetical gap coincides with the actual extracted gap. A least square fit and the Levenberg–Marquardt algorithm may be utilized in the adjustment [16]. Finally, the parameters of the creep compliance are obtained. They are listed in Table I.

Based on this creep compliance, the measured capacitance and deflection of the fabricated varactor are plotted in Figs. 4 and 5, respectively, and are compared to the simulation results. The measured capacitance and deflection in the first state is shown in the biased curve. The unbiased curve represents the

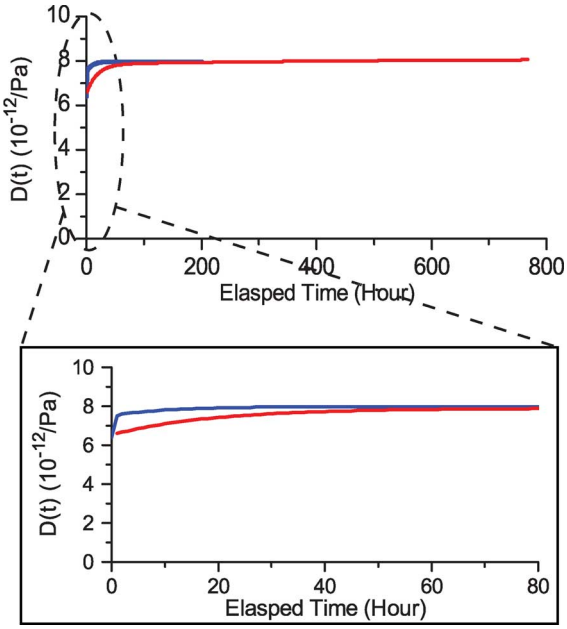

Fig. 3. Creep compliance extracted from the 760-h measurement (red line in online version). This creep compliance is employed in all simulations in this work. It is in agreement with the creep compliance reported in [12] (blue line in online version).

TABLE I
PARAMETERS OF CREEP COMPLIANCE

E_0*	E_1	τ_1*	E_2	τ_2
151.508	797.397	18.343	3996.11	477.016

* E_i is in GPa and τ_i is in hours.

data measured in the second state. It is noted that the evolution of the capacitance can be divided into two regions. In the first region, between 0–70 h, the capacitance increases rapidly, while in the second region, the slope approximates a constant. A slight discrepancy can be found in the unbiased curve between 0–50 h. This small peak may be related to the residual stress and/or measurement errors. The simulated S-parameters of this varactor shunt to a 50-Ω transmission line at 0, 10, 100, and 760 h can be found in Fig. 6.

This CAD model shows excellent consistency with measurements of both the biased and unbiased curves within the span of the measured creep compliance. It reflects the viscoelastic behavior of the primary and secondary creep, and is capable of calculating the response of RF-MEMS devices to an arbitrary input based on the measured creep compliance. It is confirmed that the legitimate period of this model is at least as long as the measured creep compliance. It may be extended to a much longer period until the occurrence of other phenomena such as creep rupture that may not be captured in the employed creep compliance. However, prediction of the effective period is beyond the scope of this paper.

III. TUNABLE RF-MEMS RESONATOR

A. Design

The presented CAD model can be utilized to show the RF behavior of a general class of RF MEMS circuits. In this section, we start with an example of a tunable RF-MEMS resonator shown in Fig. 7. This resonator consists of a 50-Ω coplanar waveguide (CPW) resonator and two analog RF-MEMS varactors symmetrically loaded at both ends of the resonator. The bias voltage is applied on the center conductor of the CPW resonator via a highly resistive SiCr bias line. The moving plate of the varactor is 200-μm

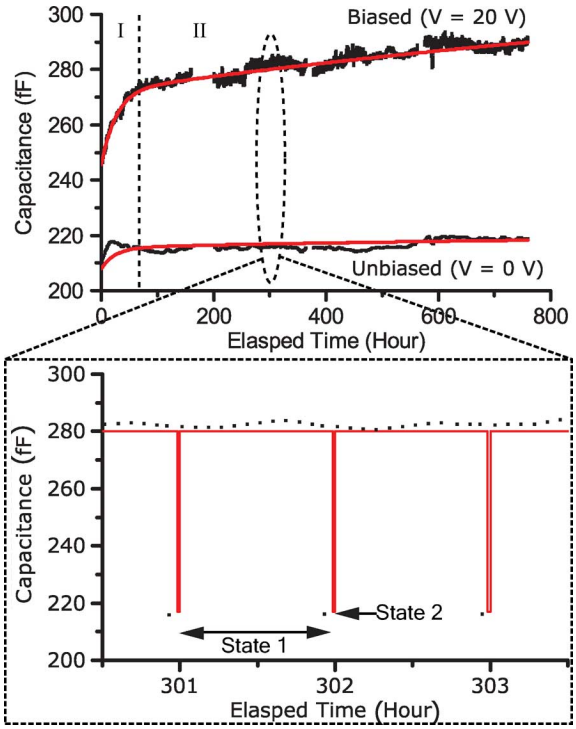

Fig. 4. Measured (black) and simulated (red in online version) capacitance of the RF-MEMS varactor over 760 h under a bi-state bias condition. Two regions can be identified.

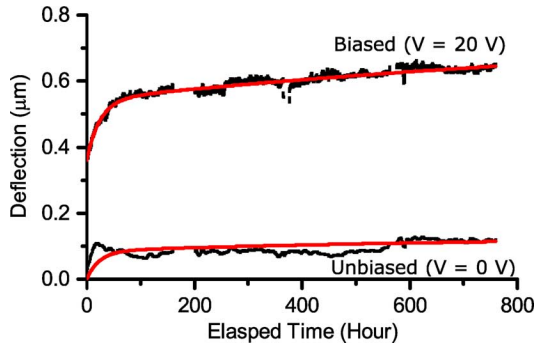

Fig. 5. Measured (black) and simulated (red in online version) deflection of the RF-MEMS varactor over 760 h under a bi-state bias condition.

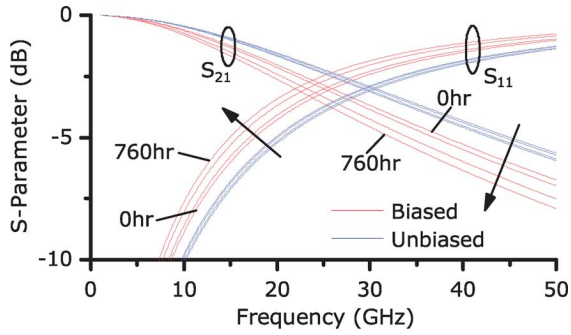

Fig. 6. Simulated S-parameters of the RF-MEMS varactor at 0, 10, 100, and 760 h under a bi-state bias condition.

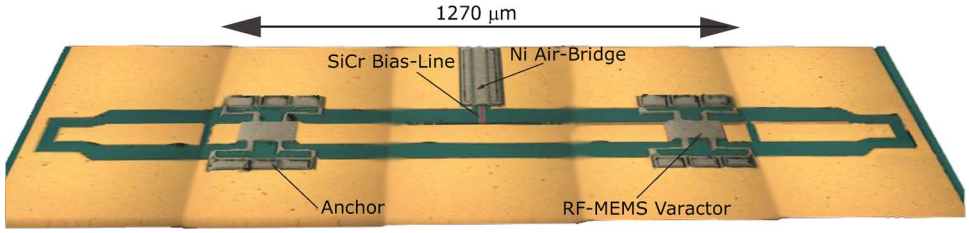

Fig. 7. Confocal microscope image of the tunable RF-MEMS resonator. The resonator consists of a 1270-μm-long CPW resonator and two analog RF-MEMS varactors. This picture is made by tiling ten images from the confocal microscope.

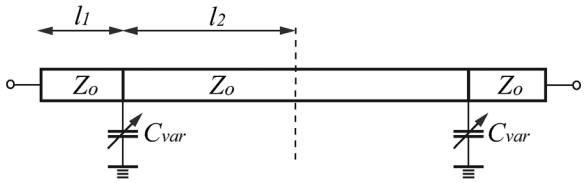

Fig. 8. Schematic of the tunable resonator loaded with two RF-MEMS varactors.

long and 120-μm wide. The length and width of the suspension beam are about 200 m and 20 μm, respectively. The thickness of the Ni varactor is 3 μm and the measured pull-in voltage is about 75 V for a gap of 4.3 μm. The anchor of the varactor is designed to enhance adhesion to the Au lines.

The equivalent circuit of this tunable resonator is shown in Fig. 8. The resonant frequency is a function of the capacitance and position of the loaded varactor [17]. It is implicitly given by

$$\overline{B}_p - \cot\theta_2 + \tan\theta_1 = 0 \tag{9}$$

where θ_1 and θ_2 are the equivalent electrical lengths of l_1 and l_2, and $\overline{B}_p$ is the normalized total shunt susceptance, which is mainly contributed by the varactors. The resonator is weakly coupled to the feed-line and ground–signal–ground pads with an open section of 30 μm. In this paper, l_1 and l_2 are 150 and 485 μm, respectively. The initial C_{var} extracted using the FEA model is 60 fF [15]. The center frequency is designed to be tuned from 29 to 32 GHz. The tuning ratio is about 10%. The simulated quality factor is about 35 [18].

B. Fabrication

The fabrication process of this tunable RF-MEMS resonator is shown in Fig. 9. The varactor is built on a p-type high-resistivity silicon substrate with a 500-nm-thick thermally grown SiO_2 film. A 100-nm-thick SiCr-film and an 1-μm-thick Au-film are sputtered and lifted off to define the CPW and electrical connections of the resonator [see Fig. 9(a)]. The anchors are then patterned through a 3-μm-thick photoresist sacrificial layer [see Fig. 9(b)]. The sacrificial layer is hard baked at 190 °C for 5 min for two reasons. First, hard baking removes the residual solvent in the photoresist and prevents it from outgassing. Second, better corner coverage of the seed layer can be obtained by rounding the sharp corners of the photoresist with hard baking. A seed layer of 50-nm sputtered Ti and 30-nm evaporated Ni is deposited on the whole sample [see Fig. 9(c)]. A 6-μm-thick photoresist layer is shaped to form the electroplating mold on the seed layer. The Ni electroplating is carried out in a nickel–sulfamate bath at a temperature of 50 °C and a pH value of 4. The average grain size is about

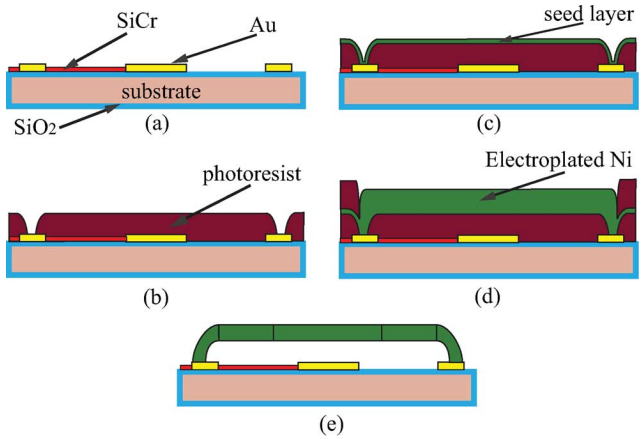

Fig. 9. Fabrication process of the tunable RF-MEMS resonator.

200 nm. A 3-μm-thick Ni layer is electroplated on the seed layer selectively based on the photoresist mold [see Fig. 9(d)]. The Ni and Ti seed layer are stripped with $HCl : H_2O = 1 : 1$ and $HF : H_2O = 1 : 20$ at room temperature, respectively, after the removal of the photoresist mold. The photoresist sacrificial layer is removed by immersion in photoresist stripper 2000 at 75 °C for 24 h. Finally, the fabrication process is completed by drying in a critical-point dryer [see Fig. 9(e)]. According to the confocal-microscope measurement, the initial gap of the varactor is approximately 4.3 μm instead of the nominal value 3 μm because of the compressive residual-stress in the Ni layer.

C. Results

In this section, the S-parameters of the tunable resonator are measured. The resonant frequency and gap of the resonator are extracted from the S-parameters. The simulation results using the presented CAD model are then compared to the measurements. The RF measurements are performed using Agilent PNA E3861C network analyzer. An on-wafer thru-reflect-load (TRL) calibration kit is employed in this measurement setup.

The tunable RF-MEMS resonator is measured using a bi-state bias condition. At the first state, a constant bias voltage V_{bias} is applied to the varactor for 60 min. At the second state, the bias voltage is removed for 1 min. This is a variation of the constant-voltage bias condition that can be found in many RF-MEMS applications. This variation provides insight into the tuning range and dynamics of the tunable RF-MEMS devices. The resonant frequencies at both biased and unbiased states are depicted in Fig. 10. A curve-fitting technique is employed to accurately estimate the resonant frequency and the measurement error. The resonant frequencies are obtained by applying

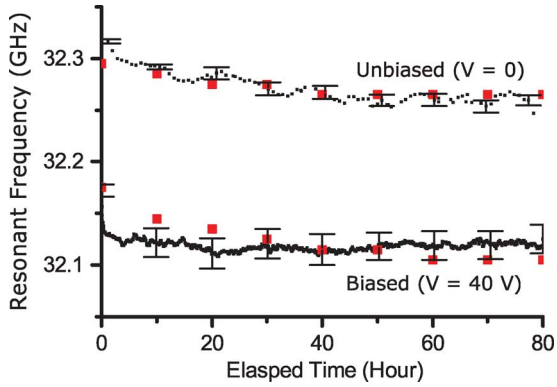

Fig. 10. Measured (black) and simulated (red in online version) resonant frequency of the tunable RF-MEMS resonator over 80 h. The error bars indicate the measurement uncertainty from the least square fit method.

Lorentzian curves to the measured S_{21} with a least square fit [19]. The corresponding uncertainty is also shown in Fig. 10.

Two regions can be identified in Fig. 10. In the first 3 h, the frequency decreases rapidly. In the second region, the slope of the frequency approximates a constant value after about 3 h. Due to the creep behavior of the two RF-MEMS varactors, the resonant frequency cannot revert to the initial frequency and is determined by the loading history. The frequency shift is up to 90 MHz, which occurs at the 80 h and 0 V. This imposes two challenges to tunable RF-MEMS filters. First, the filter may drift away from the desired frequency even though the designed voltage is applied. Second, the filter may not be able to cover the desired band after a long period of operation. For a bias voltage of 0–40 V, the resonator tunes from 32.17 to 32.35 GHz at $t = 0$. The range shifts to 32.11–32.26 GHz after operation of 80 h. The change of the resonant frequency is expected to be even greater if the full tuning range of the varactors (0–75 V) is used.

The gap of the varactor is depicted in Fig. 11. This gap is extracted from the measured S-parameters using FEA tools [15], [18]. The parasitics and fringing fields are included in the FEA extraction. It is observed that the gap shifts up to 0.12 μm in 80 h.

The CAD model can be used to simulate the time-dependent resonant frequency and gap of the resonator at both the biased and unbiased states, as shown in Figs. 10 and 11. The creep compliance in Fig. 3 is employed in this simulation. Thus, this creep compliance is obtained independently from the resonator measurement. In addition, the creep compliance has been obtained from varactors with pull-in voltages of 44 V, while the varactors in the resonators have a pull-in voltage of 75 V. As discussed in Section III-B, this resonator has an initial gap of about 4.3 μm instead of the nominal value of 3 μm because of the residual stress in the Ni layer. Hence, the pull-in voltage is elevated. Good agreement between the CAD model and the measurement is obtained. The differences are due to the fact that the varactors used to extract the CAD model and the RF MEMS resonators were fabricated 12 months away. The fabrication tolerances commonly found in MEMS fabrication during this time period explain the small differences observed.

D. Duty Factor

In some practical applications, the RF-MEMS devices may not be operated at a constant bias for a long time. Besides a constant voltage, the common bias waveforms include sawtooth waves and square waves of various duty factors. The effect of the duty factor in the input waveform can also be investigated using the proposed CAD model. In the duty factor simulation, the creep compliance in Fig. 3 is used. The duty factor of the aforementioned bi-state bias condition is adjusted to 25%, 50%, and 99%, respectively. Its period remains at 1 h.

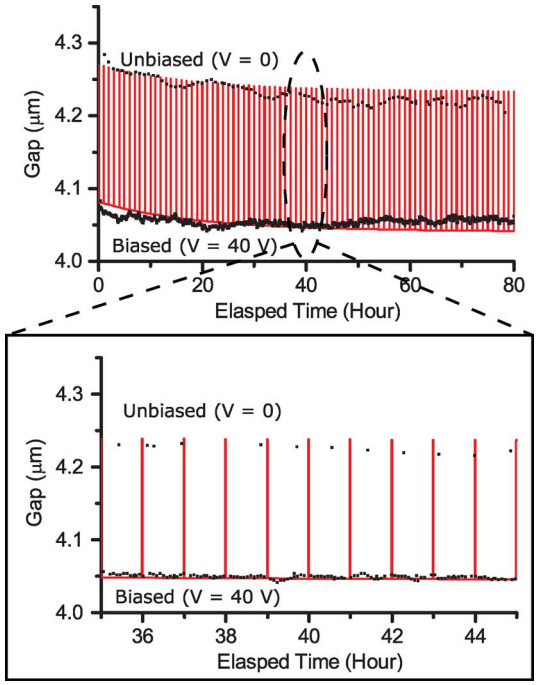

Fig. 11. FEA-extracted (black) and the simulated (red in online version) gap of the tunable RF-MEMS resonator. In the simulation, the experimentally extracted creep compliance is used in the presented CAD model.

The simulation results of the inputs of different duty factors are shown in Fig. 12. For clarity, the upper and lower bounds of the gap are indicated with the arrows on the right. It is observed that the creep deformation is a function of the duty factor. For the biased state, the deformation at the 80 h in the 99% case is 0.05 μm, whereas in the 25% case, it is only 0.02 μm. Similar deformation behavior can be also found at the unbiased state. There are two facts that cause the reduced deformation at low duty factors in Fig. 12. First, the creep deformation is increased according to the duration of the biased state. The total deformation is accumulated in each cycle. Thus, at higher duty factors, the deformation accumulation is faster. Second, strain recovery takes place in the unbiased state. Strain recovery is the process that the material returns to its original state against creep deformation after the applied force is removed. Significant strain recovery is reported in nanocrystalline metals at room temperature [20]. In the 99% case, the duration of the unbiased state is very short and the recovery is negligible. However, the recovery is more pronounced at lower duty factors as the 25% and 50% cases shown in Fig. 12. The creep deformation is reduced slightly at the unbiased state. Therefore, only a portion of the deformation is accumulated in each cycle and the total deformation increases in a lower rate. It is also shown that both creep deformation and strain recovery may need to be considered in the evaluation of the long-term behavior of RF-MEMS devices.

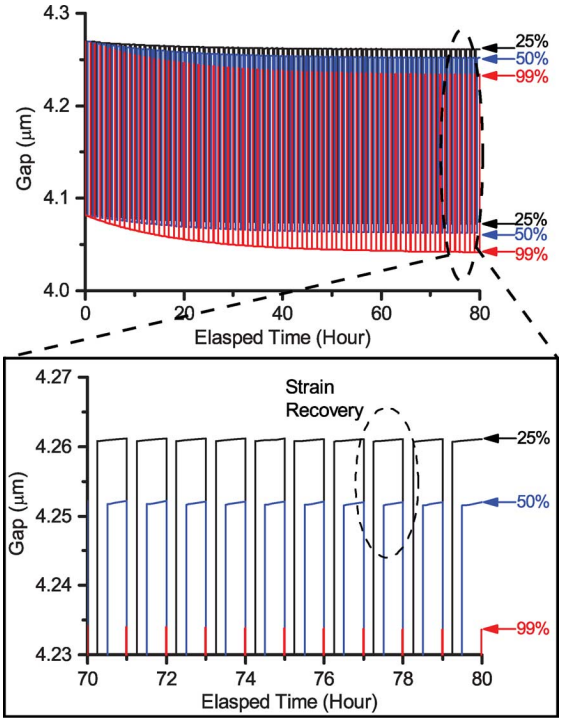

Fig. 12. Simulated gap of the tunable RF-MEMS resonator when the duty factor is 25% (black), 50% (blue in online version), and 99% (red in online version), respectively. The arrows on the right indicate the upper and lower bounds of the gap.

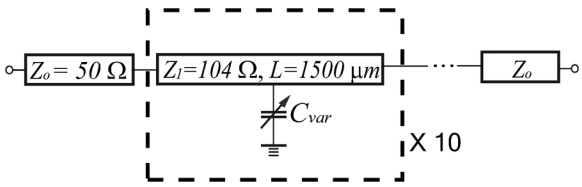

Fig. 13. Schematic of distributed RF-MEMS phase shifter. A CPW transmission line is loaded with ten RF-MEMS varactors with equal spacing.

IV. RF-MEMS Phase Shifter

The second example presented here is an analog RF-MEMS phase shifter. The phase shifter is implemented in ADS using the presented creep CAD model. This distributed MEMS phase shifter consists of an 1.5-cm-long CPW on a quartz substrate $(\epsilon_r = 3.8)$ and ten equally spaced RF-MEMS varactors, as shown in Fig. 13. The width and spacing of this CPW is 150 and 200 μm, respectively, resulting in a characteristic impedance of 104 Ω. The effective characteristic impedance of this MEMS phase shifter ranges from 48 to 52 Ω in the tuning range of these varactors. The design equations can be found in [21]. The area and spring constant of these varactors are 40 000 μm^2 and 51 N/m. The initial gap is 4.3 μm. The suspension beam design is identical to the varactor in Section III.

A sawtooth bias waveform is applied to the varactors in order to study the creep behavior of this phase shifter in scanning applications such as phase-array antennas. This input waveform starts at 0 V and increases linearly to 65 V with a period of 1 s. For comparison, the pull-in voltage of the varactor is 75 V. The simulated capacitance, as well as the input waveform, are shown in Fig. 14. Two observations can be made in Fig. 14 regarding creep. First, the change of the capacitance over time is affected by the input waveform. Compared to Fig. 4, region I lasts a shorter amount of time and the slope in region II is lower because of the sawtooth waveform. Second, the input waveform and the capacitance are synchronized.

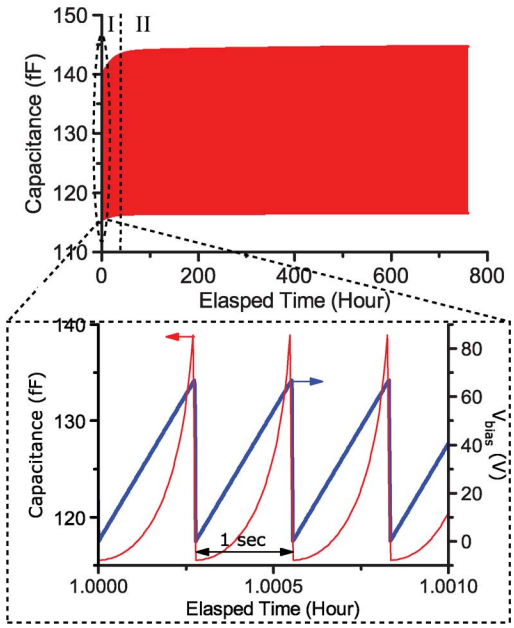

Fig. 14. Simulated capacitance of the varactors in the RF-MEMS phase shifter. The phase shifter is loaded with a sawtooth bias waveform.

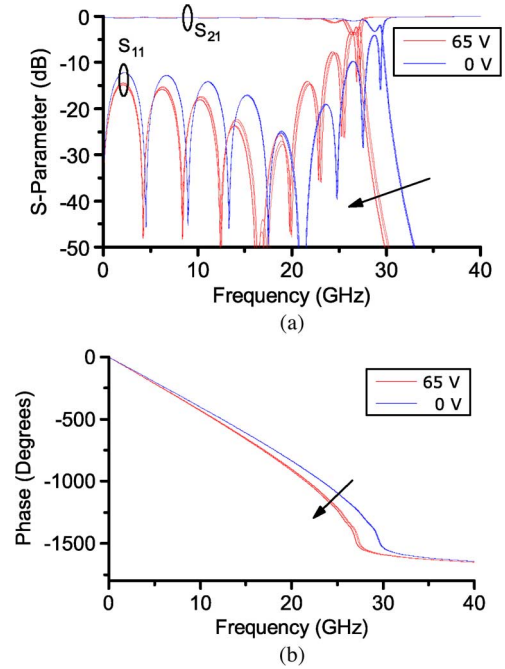

Fig. 15. Simulated: (a) magnitude and (b) phase of the RF-MEMS phase shifter at the 0, 10, 100, and 760 h under a sawtooth bias waveform of 0–65 V.

The simulated S-parameters and phases are depicted in Fig. 15 to show the creep behavior of this distributed MEMS phase shifter under the sawtooth excitation. The simulated S-parameters indicate that insertion/return loss are degraded slightly and the Bragg frequency of this phase shifter is lowered

in its long-term operation of 760 h. The phase shift at 20 GHz is increased by 14.3° when the applied voltage is 65 V due to creep, while the phase shift at $V_{\rm bias} = 0$ is raised by 2.9° after 760 h.

V. Conclusion

A CAD model for creep in RF-MEMS devices is presented and is demonstrated to accurately describe their long-term behavior. Based on the creep compliance, the time-dependent gap and capacitance of an RF-MEMS varactor under arbitrary voltage input can be calculated using this model. This CAD model is validated with experimental data for 760 h and very good consistency is obtained. The creep behavior of a tunable RF-MEMS resonator has been characterized using direct RF measurements and compared to the presented model. The evolution of resonant frequency and tuning range under a bi-state bias condition over 80 h are presented. The resonant frequency and the varactor gap shifted by 90 MHz and 0.12 μm, respectively. The effects of the duty factor of the bias condition is studied. It is shown that the behavior of the RF-MEMS devices under certain input waveforms may be affected by both creep deformation and recovery. A simulation of a distributed RF-MEMS phase shifter operated using a sawtooth input is carried out using this model. The simulated S-parameters and phase of this phase shifter are obtained. The effectiveness and usefulness of this model is demonstrated with the tunable RF-MEMS resonator and the RF-MEMS phase shifter. This model may be utilized to perform simulations on various kinds of RF-MEMS devices and higher level systems. It may have critical value to designers of RF-MEMS devices/circuits with high reliability.

References

[1] W. A. de Groot, J. R. Webster, D. Felnhofer, and E. P. Gusev, "Review of device and reliability physics of dielectrics in electrostatically driven MEMS devices," *IEEE Trans. Device Mater. Rel.*, vol. 9, no. 2, pp. 190–202, Jun. 2009.

[2] A. Hariri, J. Zu, and R. B. Mrad, "Modeling of wet stiction in micro-electromechanical systems (MEMS)," *J. Microelectromech. Syst.*, vol. 16, no. 5, pp. 1276–1285, Oct. 2007.

[3] A. Somà and G. D. Pasquale, "MEMS mechanical fatigue: Experimental results on gold microbeams," *J. Microelectromech. Syst.*, vol. 18, no. 4, pp. 828–835, Aug. 2009.

[4] H. Kwon, D.-J. Choi1, J.-H. Park, H.-C. Lee, Y.-H. Park, Y.-D. Kim, H.-J. Nam, Y.-C. Joo, and J.-U. Bu, "Contact materials and reliability for high power RF-MEMS switches," in *IEEE Int. Microelectromech. Syst. Conf.*, Jan. 2007, pp. 231–234.

[5] D. J. Vickers-Kirby, R. L. Kubena, F. P. Stratton, R. J. Joyce, D. T. Chang, and J. Kim, "Anelastic creep phenomena in thin metal plated cantilevers for MEMS," in *Mater. Res. Soc. Symp.*, 2001, vol. 657, pp. EE2.5.1–EE2.5.6.

[6] K. Tuck, A. Jungen, A. Geisberger, M. Ellis, and G. Skidmore, "A study of creep in polysilicon MEMS devices," *J. Eng. Mater. Technol.*, vol. 127, pp. 90–202, Jan. 2005.

[7] M. van Gils, J. Bielen, and G. McDonald, "Evaluation of creep in RF MEMS devices," in *IEEE Int. Thermal, Mech., Multi-Phys. Simulation and Experiments in Micro-Electron. Micro-Syst. Conf.*, Apr. 2007, pp. 1–6.

[8] I. Chasiotis, C. Bateson, K. Timpano, A. McCarty, N. Barker, and J. Stanec, "Strain rate effects on the mechanical behavior of nanocrystalline Au films," *Thin Solid Films*, vol. 515, no. 6, pp. 3183–3189, Feb. 2007.

[9] X. Yan, W. L. Brown, Y. Li, J. Papapolymerou, C. Palego, J. C. M. Hwang, and R. P. Vinci, "Anelastic stress relaxation in gold films and its impact on restoring forces in MEMS devices," *J. Microelectromech. Syst.*, vol. 18, no. 3, pp. 570–576, Jun. 2009.

[10] H.-H. Hsu and D. Peroulis, "A viscoelastic-aware experimentally-derived model for analog RF MEMS varactors," in *IEEE Int. Microelectromech. Syst. Conf.*, Jan. 2010, pp. 783–786.

[11] R. S. Lakes, *Viscoelastic Materials*. New York: Cambridge Univ. Press, 2009.

[12] H.-H. Hsu and D. Peroulis, "An experimental investigation on viscoelastic behavior in tunable planar RF-MEMS resonators," in *IEEE MTT-S Int. Microw. Symp. Dig.*, May 2010, pp. 1150–1153.

[13] H. F. Brinson and L. C. Brinson, *Polymer Engineering Science and Viscoelasticity an Introduction*. New York: Springer, 2008.

[14] Advanced Design System (ADS). Agilent Technol., Santa Clara, CA, 2005. [Online]. Available: http://www.agilent.com

[15] Ansoft Maxwell 3D. ver. 12, ANSYS Inc., Canonsburg, PA, 2008. [Online]. Available: http://www.ansoft.com

[16] Mathematica. ver. 6, Wolfram Res., Champaign, IL, 2007. [Online]. Available: http://www.wolfram.com

[17] A. Abbaspour-Tamijani, L. Dussopt, and G. M. Rebeiz, "A millimeter-wave tunable filter using MEMS varactor," in *IEEE MTT-S Int. Microw. Symp. Dig.*, Jun. 2003, pp. 1785–1788.

[18] Ansoft HFSS. ver. 10, ANSYS, Canonsburg, PA, 2008. [Online]. Available: http://www.ansoft.com

[19] P. J. Petersan and S. M. Anlage, "Measurement of resonant frequency and quality factor of microwave resonator: Comparison of methods," *J. Appl. Phys.*, vol. 84, pp. 3392–3402, 1998.

[20] J. Rajagopalan, H. Jong, and M. T. A. Saif, "Plastic deformation recovery in freestanding nanocrystalline aluminum and gold thin films," *Science*, vol. 315, pp. 1831–1834, 2007.

[21] G. M. Rebeiz, *RF MEMS: Theory, Design, and Technology*. New York: Wiley, 2003.

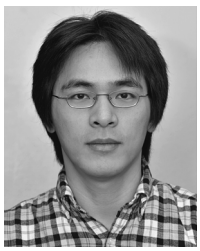

Hao-Han Hsu (S'10) received the B.S. and M.S. degrees in electrical engineering from National Tsing Hua University, Hsinchu, Taiwan, in 2001 and 2002 respectively, and is currently working toward the Ph.D. degree in electrical and computer engineering at Purdue University, West Lafayette, IN.

He possesses ten years of experience in his field of expertise. His current research interests include design, fabrication, and application of high-quality and highly reliable RF-MEMS devices.

Mr. Hsu was the recipient of the Student Paper Award of the 2011 IEEE Topical Meeting on Silicon Monolithic Integrated Circuits in RF Systems.

Dimitrios Peroulis (S'99–M'03) received the Ph.D. degree in electrical engineering from The University of Michigan at Ann Arbor, in 2003.

Since August 2003, he has been with Purdue University, West Lafayette, IN, where he currently leads a group of 15 Ph.D. students in a variety of research projects in the areas of MEMS for RF, sensing and power harvesting applications, as well as RF identification (RFID) sensors for the health monitoring of sensitive equipment. He possesses nine years experience in his field of expertise and has led a variety of projects funded by the U.S. Air Force, Army, and Defense Advanced Research Projects Agency (DARPA) in these areas. He currently leads two DARPA projects at Purdue University, which focus on very high-quality ($Q > 1000$) RF tunable filters (Evanescent Filter Cavities for Analog Spectral Processing) and developing sophisticated models for understanding the failure mechanisms of MEMS devices (University Center on MEMS/NEMS S&T Fundamentals Program). In addition, he leads an Air Force project on RFID MEMS sensors and two National Science Foundation (NSF) projects on wireless networks. He has authored or coauthored over 40 refereed journal and conference publications in the areas of microwave integrated circuits and antennas. He is a member of the Center of Wireless Systems and Applications and the Birck Nanotechnology Center, Purdue University.

Dr. Peroulis was a six-time recipient of the Outstanding Teacher Award of Purdue University. He was also a two-time recipient of the Student Paper Award of the 2001 and 2002 IEEE Microwave Theory and Techniques Society (IEEE MTT-S) International Microwave Symposium (IMS).